Accepted manuscript. Published in International Journal of Solids and Structures (2024). Version of record: https://doi.org/10.1016/j.ijsolstr.2024.113191. © 2024. This manuscript version is made available under the CC-BY-NC-ND 4.0 license https://creativecommons.org/licenses/by-nc-nd/4.0/

An Analytical Model for the Bending and Reaction Force of Hygroscopic Bilayers upon Water Adsorption

Mohammadali Behboodi[1], Mehdi Eskandari-Ghadi[2], Wenjie Xia[3], Yida Zhang[1*]

Abstract

Hygroscopic bilayers replicating the morphing capability of plants upon hydration (e.g., pinecone scales, Chiral seed pods) have gained much attention in robotics and material science research in the past decade. Due to variations in humidity, hygroscopic bilayers – comprising a passive substrate and an active porous coating – can convert the chemical potential difference of adsorbate species between the surrounding environment and the pore space to mechanical energy, resulting in development of curvature and forces. In this paper, we present a closed-form analytical model that considers the pore structure of the active layer for predicting the morphing of hygroscopic bilayers subjected to adsorption. For free-end cases, the curvature evolution as function of relative humidity is predicted by combining a bilayer beam theory and a linear surface poroelasticity model for the active porous layer. For fixed-end scenarios, the reaction force generated by the bilayer is predicted using Castigliano's second theorem with the same constitutive model. For validation, we consider two types of hydroscopic bilayers with microporous and mesoporous coatings, as tested by Boudot et al. (2016). A new isotherm equation is introduced to capture the adsorption characteristics of mesoporous media at all humidity levels. The predicted curvature and reaction force curves compared well against the experimental data. Finally, the effects of substrate Young's modulus and the coating's thickness on the response of the bilayer are studied. The proposed model offers

[1] Department of Civil, Environmental and Architectural Engineering, University of Colorado Boulder, Boulder, CO, USA
[2] PacifiCorp, Salt Lake City, UT, USA
[3] Department of Department of Aerospace Engineering, Iowa State University, Ames, IA, USA
[*] Corresponding author. E-mail address: yida.zhang@colorado.edu (Yida Zhang).

straightforward mechanistic description of hydroscopic bilayers, thereby aiding in the future optimization and design of these systems for engineering applications.

Keywords: hygroscopic, actuator, bilayer, adsorption, poromechanics, porous media.

1. Introduction

Many natural or engineered soft-porous materials exhibit prominent deformation in response to the adsorption of guest molecules (water, CO_2, N_2). Plant systems harness hygroscopic movement to gain advantages during seed dispersal. Examples include the opening up of tightly packed pinecone upon the reduction of ambient humidity (Reyssat and Mahadevan, 2009), and the twisting and opening of Chiral seed pods when dried (Armon et al., 2011). These movements originated from the sorption-induced deformation of cellulose nanofibrils in plant tissues. Natural hygromorphs has become a source of inspiration of numerous innovations in materials engineering (Harrington et al., 2011; Li and Wang, 2016; Montero de Espinosa et al., 2017; Sydney Gladman et al., 2016). Sorption-driven soft actuators have been also applied to develop smart workout suits with vents that open and close as athletes sweat (Wang et al., 2017), artificial muscles in robotic applications (Higueras-Ruiz et al., 2021), and moisture-responsive architectures (Menges, 2012).

Among them, hygroscopic bilayer is perhaps the simplest type of sorption-driven actuators. It consists of a non-sorptive substrate layer coated by a porous, adsorptive layer on the top. As the relative humidity (RH) in the environment rises, the moisture-responsive layer draws water molecules into its pores, subsequently experiences a large magnitude of swelling due to the modification of pore-scale forces. For the non-sliding contact between layers, such expansion in the responsive layer leads to the bending of the bilayer system (Fig. 1). Different hygroscopic bilayers have been studied based on the choice of coating material, substrate, and geometry. Reyssat and Mahadevan (2009) created a biomimetic hygroscopic bilayer with paper as the responsive material and plastic polymer as the substrate, mimicking pinecone scale movement driven by humidity. They found that the curvature response of the bilayer depends on the thickness and modulus ratios of its layers. Correa et al. (2020) designed 4-D printed bilayers with the responsive layer printed in various patterns to study and replicate the biaxial (longitudinal and transverse)

curvature development observed in Bhutan pine scales. Boudot et al. (2016) devised two types of porous bilayers and compared their mechanical performances during humidity change. The first type had a microporous xerogel silica coating with pore size smaller than 2 nm, while the second type had a mesoporous silica coating with an average pore size of 5.5 nm, both deposited on an inert polyimide substrate. The bilayers are able to walk down a tilted rack as the surrounding humidity oscillated. Shin et al. (2018) fabricated hygrobots with different geometries to achieve locomotion without external power by crawling on moist surfaces. Recently, Zhao et al. (2014) synthesized a porous polymer strip that undergoes rapid, large, and reversible deformation, forming a spiral shape when exposed to solvent vapors.

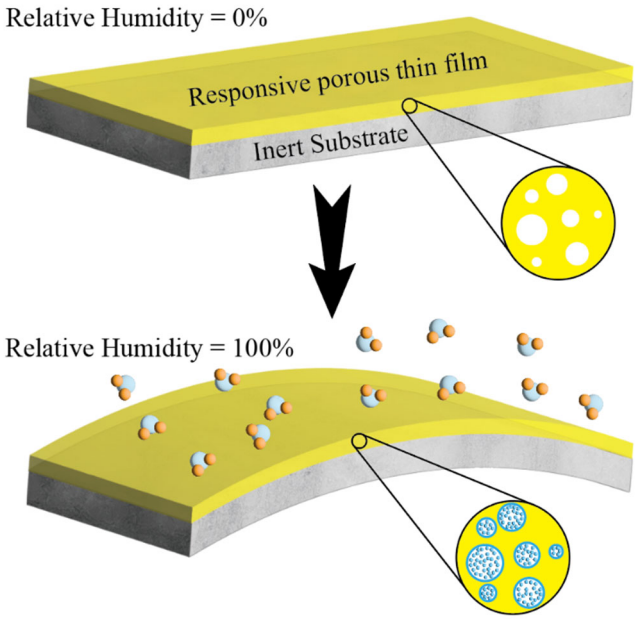

Fig. 1. A hygroscopic bilayer, consisting of an inert substrate and a responsive thin film, undergoes bending as a result of adsorption of water molecules due the relative humidity rise.

To optimize the design of hygroscopic structures, it is imperative to employ modeling that integrates structural mechanics and the inherent characteristics of sorptive porous materials. Khoshtinat et al. (2023) combined experiments, analytical methods, and finite element simulations to study curvature changes in hygroscopic bilayers during moisture variations. Their finite element simulation, employing linear elasticity with a hydroscopic expansion coefficient (analogous to the thermal expansion coefficient),

closely matched experimental findings, while the beam-theory based (Timoshenko, 1925) analytical calculation showed disparities. Krüger et al. (2021) studied and modeled a series of 4D-printed bilayer structures. Although they have adapted Timoshenko's analysis of bi-metal thermostats for their new geometries, the estimation of the swelling strain of the active layer — an essential input for their model — has to be sourced from experimental data due to the absence of an appropriate constitutive model for the porous layer.

Several constitutive theories have been developed for modeling the mechanosorptive behavior of soft materials. For polymers such as hydrogels, the sorption-induced deformation is seen as a result of the intrusion of solvent molecules (e.g. water) into the polymer's 3D network which is thermodynamically equivalent to mixing (Hong et al., 2008). Therefore, in modeling hydrogels, the entire solid is treated as a single-phase material obeying finite-strain thermoelasticity, and sorption-swelling is introduced through Flory and Rehner (1943)'s free energy of mixing (Alameen et al., 2023; Suo, 2007; Zhao et al., 2008). Alternative to this chemomechanical approach is the poromechanics approach, where the material is treated as a deformable solid skeleton with many void spaces (pores) that host and transmit fluids. Upon adsorption, adsorbate molecules become trapped or bonded to the pore surfaces (Dąbrowski, 2001). Vandamme et al. (2010) modified the thermodynamical formulation of Biot's Poroelasticity (Biot, 1941; Coussy, 2004) to include an extra surface energy term in the energy conservation, allowing for the calculation of surface stress and subsequently introducing the dependency of solid deformation on the adsorbate concentration on the pore surface. Building upon this work and inspired by Gibbs' surface excess concept (DeHoff, 2006), Zhang (2018) developed a surface poromechanics (SP) theory that treats sorptive porous media as a three-phase mixture consisting of solid, fluid, and solid-fluid interface. Through mixture theory, Zhang (2018) rigorously showed that surface stress and surface area is a pair of work-conjugated variables that contributes to the energetics of the porous skeleton. As adsorption reduces

the solid-fluid surface energy (DeHoff, 2006), swelling is therefore a natural outcome of the relaxation of the pre-installed surface stress along the solid skeleton, a phenomenon usually referred to as the Bangham's effect (Bangham and Fakhoury, 1928). Further specifying the energy potentials permits the recovery of two-way coupled adsorption-deformation constitutive models for generic material systems from hard to soft, isotropic to anisotropic, microporous to macroporous (Eskandari-Ghadi and Zhang, 2021, 2022; Zhang, 2018; Zhou et al., 2021).

In this context, the purpose of this study is to 1) develop an analytical model for the deformation and force generation of generic bilayer systems driven by a misfit strain between the two layers, and 2) specialize the solution for hygroscopic bilayers by integrating it with surface poromechanics. This paper is arranged as follows: the structural modeling of stimuli-responsive bilayer is laid out in Section 2. Section 3 contains a linear surface-poroelastic model and its adaptation for thin porous layers, and different adsorption isotherms suitable for microporous and mesoporous materials. Section 5 examines the performance of the model by comparing the experimental curvature and force output of the bilayer measured by Boudot et al. (2016) with our model predictions. Section 6 discusses the shape evolution of the bilayer at different humidity levels and a parametric study investigating the effect of elastic modulus and layer thickness on the bilayer response. Section 7 summarizes the primary findings and prospective avenues for further explorations.

2. Mechanical model for stimuli-responsive bilayers

Let us start by considering a bilayer strip consisting of an inert layer (substrate) with a thickness of H and a responsive layer (coating) with a thickness of h adhered to the substrate, as shown in Fig. 2.

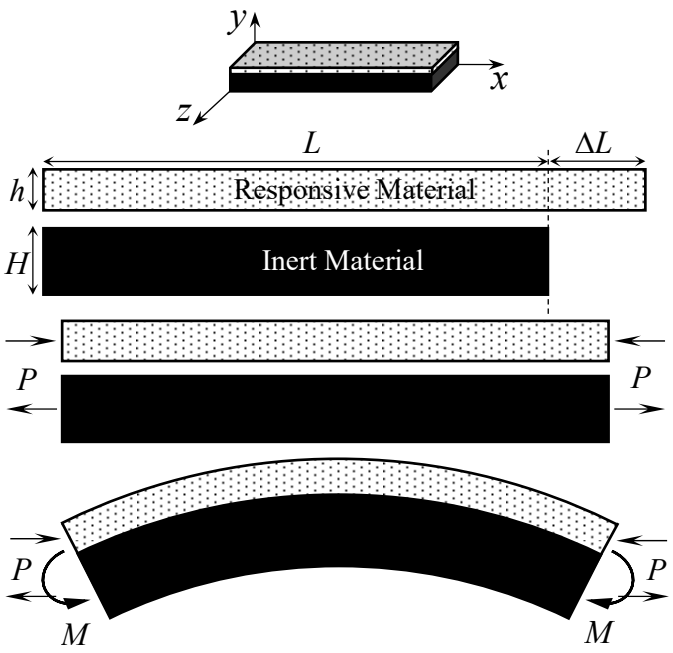

Fig. 2. Clyne's bilayer beam model and the sequences of bending development due to a misfit strain.

Assume an external stimulus (e.g., temperature change, humidity change) causing an axial (x – direction) extension of ΔL in the responsive layer. The misfit strain is defined as $\Delta\varepsilon = \Delta L / L$ where L is the initial length of the bilayer. The curvature development along the bilayer due to the external stimulus can be idealized as a two-step problem assuming no adhesive bond between the layers (Clyne, 1995). First, the length difference between the two layers is removed using a pair of forces P equal and in opposite directions applied in the middle of each layer, respectively. Second, the couple introduced by P in the first step shall be compensated by applying a moment $M = P(H + h)/2$ in the reverse direction at both ends of the beam, resulting in a constant curvature along the bilayer. Considering the equilibrium of forces and moments and apply the elastic Euler-Bernoulli beam theory, the curvature change $\Delta\kappa$ of the beam arising from a misfit strain $\Delta\varepsilon$ in the top responsive layer can be derived (Clyne, 1995):

$$\Delta\kappa = \frac{6E_tE_b(h+H)hH\Delta\varepsilon}{E_t^2h^4 + 4E_tE_bh^3H + 6E_tE_bh^2H^2 + 4E_tE_bhH^3 + E_b^2H^4} \quad (1)$$

where E_t and E_b are Young's modulus of the top responsive and the bottom inert layers, respectively. As shown in Fig. 2, each layer is under isotropic in-plane ($x-z$) stress state and zero out-of-plane stress σ_y

$$\sigma_x = \sigma_z ; \sigma_y = 0; \varepsilon_x = \varepsilon_z \tag{2}$$

Thus, the strain in $x-$direction is also affected by the stress in $z-$direction, and the Young's modulus of the each layer in Eq. (1) must be replaced by

$$E_t' = \frac{E_t}{1-\nu_t}; E_b' = \frac{E_b}{1-\nu_b} \tag{3}$$

where ν_t and ν_b are Poisson's ratios of the top and the bottom layers, respectively. It is worth keeping in mind that Clyne's solution assumes zero shear stress between the two layers and is based on Euler-Bernoulli beam theory, which considers small strains and small rotations. Despite these assumptions, Eq. (1) remains quite robust, as will be demonstrated in Section 4.

Another common configuration to test the performance of stimuli-responsive bilayers is to constrain the boundaries and measure the reactive forces. In the experimental study of Boudot et al. (2016), the initially curved (due to manufacturing process) and dry hygroscopic bilayer strip was anchored at its midpoint in the test chamber, with one of its free end rested against a microforce sensing probe to register the force generation during humidity increments. Fig. 3 depicts an idealized schematic for this setup: a bilayer beam with an initial curvature of κ_0 is configured as a cantilever. Its curvature is expected to reduce due to the development of $\Delta\varepsilon$ in the top layer. A counteracting horizontal force F is introduced to restrict the lateral displacement of the tip (i.e., $\delta_H = 0$). Given the linear elastic nature of the beam, the principle of superposition applies, and the compatibility equation governs that:

$$\delta_H^{St} = \delta_H^F \tag{4}$$

where δ_H^{St} and δ_H^F are the tip lateral displacement due to an external stimulus and that caused by the force F, respectively.

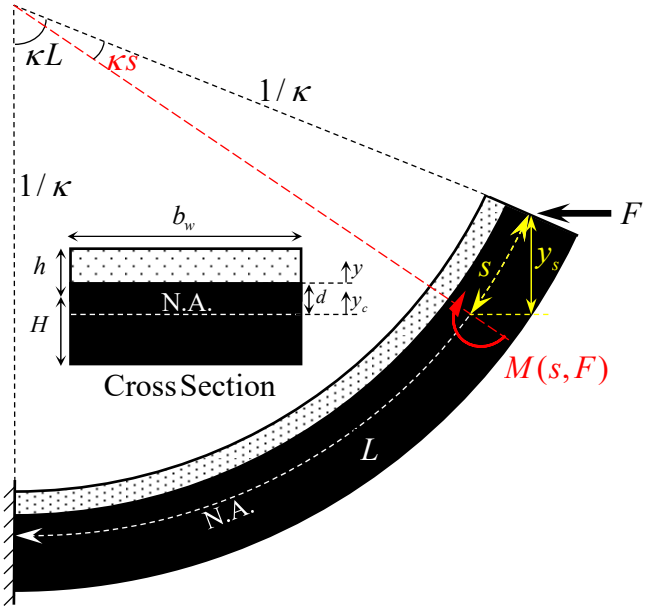

Fig. 3. An initially curved cantilever bilayer beam and the reaction force generated by misfit strain Δε.

Assuming the absence of F, the horizontal displacement of the free end of the beam induced by external stimuli can be approximated by

$$\delta_H^{St} = \frac{\sin(\kappa L)}{\kappa} - \frac{\sin(\kappa_0 L)}{\kappa_0} \tag{5}$$

where L is the total length of beam; κ is the curvature of the beam assuming free-end condition

$$\kappa = \kappa_0 - \Delta\kappa \tag{6}$$

and $\Delta\kappa$ is calculated by Eq. (1).

On the other hand, we calculate the tip lateral displacement induced by F through Castigliano's second theorem. This theorem states that, in an elastic structure under n concentrated forces, the displacement

δ_i at the point i at which the force F_i is acting on is equal to the partial derivative of strain energy stored in the structure $U_s(F_1,...,F_n)$ with respect to the external force F_i (Hibbeler, 2006):

$$\delta_i = \frac{\partial U_s(F_1,...,F_n)}{\partial F_i} \tag{7}$$

where i goes from 1 to n. For the slender bilayer structure considered here, the total energy storage is contributed by the moment along the length (Hibbeler, 2006).

$$U_s = \int \frac{M^2(s,F_1,...,F_n)}{2EI} ds \tag{8}$$

where s is a coordinate that traces the length of the structural member; M is the internal moment; I is the moment of inertia of the beam's cross section with respect to neutral axis. Substituting Eq. (8) into Eq. (7) gives:

$$\delta_i = \int \frac{\partial M(s,F_1,...,F_n)}{\partial F_i} \frac{M(s,F_1,...,F_n)}{EI} ds \tag{9}$$

Now we specialize Eq. (7) for the composite beam cross section and the configuration depicted in Fig. 3. There is a single horizontal force F at the free end of the cantilever, giving a moment distribution of:

$$M(s,F) = F y_s(s) \tag{10}$$

where

$$y_s(s) = \frac{\cos(\kappa L - \kappa s) - \cos(\kappa L)}{\kappa} \tag{11}$$

Substituting Eqs. (10) and (11) into (9) gives:

$$\delta_H^F = \frac{F}{S\kappa^2} \int_0^L \left(\cos(\kappa L - \kappa s) - \cos(\kappa L)\right)^2 ds \tag{12}$$

where S is the equivalent flexural rigidity of the composite beam (see the cross section in Fig. 3)

$$S = b_w \int_{-H-d}^{h-d} E(y) y_c^2 \, dy_c = b_w E_b' \left(\frac{y^3}{3} \right)_{-H-d}^{-d} + b_w E_t' \left(\frac{y^3}{3} \right)_{-d}^{h-d} = b_w E_t' h \left(\frac{h^2}{3} - hd + d^2 \right) + b_w E_b' H \left(\frac{H^2}{3} + Hd + d^2 \right) \tag{13}$$

and d is the distance between the neutral axis of the composite cross-section and the interface line:

$$d = \frac{\int y \, E(y) \, dA}{\int E(y) \, dA} = \frac{b_w E_b' \int_{-H}^{0} y \, dy + b_w E_t' \int_{0}^{h} y \, dy}{b_w E_b' \int_{-H}^{0} dy + b_w E_t' \int_{0}^{h} dy} = \frac{-E_b' H^2 + E_t' h^2}{2(E_b' H + E_t' h)} \tag{14}$$

Note that, for the scenario of isotropic in-plane stress, the modified Young's modulus in Eq. (3) was used. Finally, combining Eqs. (4), (5), and (12) gives the reaction force generated by the bilayer beam in Fig. 3.

$$F = S\kappa^3 \frac{\left(\frac{\sin(\kappa L)}{\kappa} - \frac{\sin(\kappa_0 L)}{\kappa_0} \right)}{\left(\kappa L + \frac{\kappa L}{2} \cos(2\kappa L) - \frac{3}{4} \sin(2\kappa L) \right)} \tag{15}$$

Eqs. (1) and (15) are derived for general bilayers without specifying the physics that drives the misfit strain $\Delta\varepsilon$. These solutions therefore work for thermal, piezoelectrical, hygroscopic, and other types of stimuli-responsive bilayers. We now shall dive into the constitutive modeling of the sorptive porous materials to focus this study on hygroscopic bilayers.

3. Constitutive model for sorptive porous materials

Upon adsorption of guest molecules, porous materials generally expand with various degrees of volumetric strain (coal ~ 3%, aerogel ~ 30%), accompanied by changes in internal structure measured by properties such as porosity, pore size distribution, and specific surface area (Bakhshian and Sahimi, 2017; Pini et al., 2009). The surface poromechanics theory was devised for explaining and modeling such ubiquitous phenomenon (Eskandari-Ghadi and Zhang, 2021; Zhang, 2018). In this theory, the solid-fluid interface is treated as an independent phase that carries mass, momentum, entropy, and energy and can

exchange these quantities with the solid and the fluid phases. Starting from the fundamental balance laws of the three-phase mixture, Zhang (2018) arrived at the free energy balance of the solid phase under isothermal and small-strain condition:

$$d\Psi_s = \boldsymbol{\sigma} : d\boldsymbol{\varepsilon} + p d\phi - \sigma^s dA_s \tag{16}$$

where Ψ_s is the Helmholtz free energy of the solid phase; $\boldsymbol{\sigma}$, $\boldsymbol{\varepsilon}$, p, and ϕ are the stress and strain tensor, fluid pressure, and the Lagrangian porosity, respectively; σ^s is surface stress which reduces to the more familiar surface energy γ for unstretchable interfaces (Shuttleworth, 1950); A_s is the specific surface area per unit reference volume. This confirms that the presence of A_s in the macroscopic expression of Ψ_s is not a constitutive assumption but a direct consequence of energy balance for solid-fluid-interface system, permitting the surface properties to affect the mechanical response of the porous solid. In this section, we shall derive an explicit expression of the misfit strain $\Delta\varepsilon$ using a simple surface poroelastic model.

Let us begin with the usual quadratic expression of Ψ_s for a linear poroelastic solid:

$$\Psi_s(\boldsymbol{\varepsilon}, \phi) = \left(\frac{\mathbf{C}^{\varepsilon}}{2} : (\boldsymbol{\varepsilon} - \boldsymbol{\varepsilon}_r) \right) : (\boldsymbol{\varepsilon} - \boldsymbol{\varepsilon}_r) + \mathbf{C}^{\varepsilon\phi} : (\boldsymbol{\varepsilon} - \boldsymbol{\varepsilon}_r)(\phi - \phi_r) + \frac{C^{\phi}}{2}(\phi - \phi_r)^2 \tag{17}$$

where $(\boldsymbol{\varepsilon}_r, \phi_r)$ denotes an arbitrary reference state for the representative elementary volume (REV); $\mathbf{C}^{\varepsilon}$, $\mathbf{C}^{\varepsilon\phi}$, and C^{ϕ} are stiffness coefficients. For an isotropic solid, they are expressed as:

$$C^{\varepsilon}_{ijkl} = (K - \frac{2G}{3} + b^2 N)\delta_{ij}\delta_{kl} + G(\delta_{ik}\delta_{jl} + \delta_{il}\delta_{jk}),\ C^{\varepsilon\phi}_{ij} = -bN\delta_{ij},\ C^{\phi} = N \tag{18}$$

where K, G, b, and N are bulk modulus, shear modulus, Biot's coefficient, and Biot's modulus, respectively. Note that the nominal stiffness of certain nanoporous materials, such as hydrogels and amorphous cellulose networks, is known to vary as these materials undergo substantial volumetric expansion with increasing humidity (Benítez et al., 2013). However, consistent with the small-strain

assumption underlying the proposed analytical solution in this study, parameters K, G, b, and N are approximated as constant here. Substituting Eq. (17) into (16) with the approximation $\sigma^s \approx \gamma$, one obtains the following constitutive relations:

$$\begin{aligned} \boldsymbol{\sigma} - \boldsymbol{\sigma}_a &= \left.\frac{\partial \Psi_s}{\partial \boldsymbol{\varepsilon}}\right|_{\phi} = \mathbf{C}^{\varepsilon} : \left(\boldsymbol{\varepsilon} - \boldsymbol{\varepsilon}_r\right) + \mathbf{C}^{\varepsilon\phi}(\phi - \phi_r) \\ p - p_a &= \left.\frac{\partial \Psi_s}{\partial \phi}\right|_{\boldsymbol{\varepsilon}} = \mathbf{C}^{\varepsilon\phi} : \left(\boldsymbol{\varepsilon} - \boldsymbol{\varepsilon}_r\right) + C^{\phi}(\phi - \phi_r) \end{aligned} \tag{19}$$

where

$$\boldsymbol{\sigma}_a = \gamma \frac{\partial A_s}{\partial \boldsymbol{\varepsilon}}, \quad p_a = \gamma \frac{\partial A_s}{\partial \phi} \tag{20}$$

are adsorption stress and pressure, respectively. We shall define the reference state in such a way that it facilitates the calibration of the model based on routine experiments. It is always convenient to consider that the *initial state* of material REV is at zero initial strain ($\boldsymbol{\varepsilon} = \mathbf{0}$) and a given initial porosity ($\phi = \phi_0$) under vacuum and stress-free ($\boldsymbol{\sigma} = \mathbf{0}, p = 0$) conditions. By selecting a reference state $(\boldsymbol{\varepsilon}_r, \phi_r)$ that satisfies

$$\begin{aligned} \mathbf{C}^{\varepsilon} : \boldsymbol{\varepsilon}_r + \mathbf{C}^{\varepsilon\phi}(\phi_r - \phi_0) &= \boldsymbol{\sigma}_{a0} \equiv \left.\left(\gamma \frac{\partial A_s}{\partial \boldsymbol{\varepsilon}}\right)\right|_{\boldsymbol{\varepsilon}=\mathbf{0}, \phi=\phi_0} \\ \mathbf{C}^{\varepsilon\phi} : \boldsymbol{\varepsilon}_r + C^{\phi}(\phi_r - \phi_0) &= p_{a0} \equiv \left.\left(\gamma \frac{\partial A_s}{\partial \phi}\right)\right|_{\boldsymbol{\varepsilon}=\mathbf{0}, \phi=\phi_0} \end{aligned} \tag{21}$$

one can rewrite Eq. (19) as:

$$\begin{aligned} \boldsymbol{\sigma} - \Delta\boldsymbol{\sigma}_a &= \mathbf{C}^{\varepsilon} : \boldsymbol{\varepsilon} + \mathbf{C}^{\varepsilon\phi}(\phi - \phi_0) \\ p - \Delta p_a &= \mathbf{C}^{\varepsilon\phi} : \boldsymbol{\varepsilon} + C^{\phi}(\phi - \phi_0) \end{aligned} \tag{22}$$

with

$$\Delta\boldsymbol{\sigma}_a = \boldsymbol{\sigma}_a - \boldsymbol{\sigma}_{a0} = \gamma\frac{\partial A_s}{\partial \boldsymbol{\varepsilon}} - \left(\gamma\frac{\partial A_s}{\partial \boldsymbol{\varepsilon}}\right)\Big|_{\boldsymbol{\varepsilon}=\mathbf{0},\phi=\phi_0}$$
$$\Delta p_a = p_a - p_{a0} = \gamma\frac{\partial A_s}{\partial \phi} - \left(\gamma\frac{\partial A_s}{\partial \phi}\right)\Big|_{\boldsymbol{\varepsilon}=\mathbf{0},\phi=\phi_0} \tag{23}$$

where symbol Δ denotes the difference between the current value and the initial value (at the initial state) of its operand. One can readily check that Eq. (22) satisfies the desired initial state ($\boldsymbol{\varepsilon}=\mathbf{0}$, $\phi=\phi_0$) at ($\boldsymbol{\sigma}=\mathbf{0}, p=0$).This model relates the stress state of a porous solid and the pore pressure to the macroscopic measures of strain and porosity (Eskandari-Ghadi and Zhang, 2022). One insight we gain from Eq. (22) is that the material can experience stress and pressure due to adsorption through changes in surface tension (via $\Delta\boldsymbol{\sigma}_a, \Delta p_a$) even at an apparently stress-free condition ($\boldsymbol{\sigma}=\mathbf{0}, p=0$).

Assuming spherical pores as microstructure of the solid skeleton, the specific surface area can be linked to porosity via (Vandamme et al., 2010):

$$A_s = \frac{3}{R_I}\phi_0^{1/3}\phi^{2/3} \tag{24}$$

where R_I is the average radius of the pores. Substituting Eq. (24) into (23) gives:

$$\Delta\boldsymbol{\sigma}_a = 0,\ \Delta p_a = \frac{2}{R_I}\phi_0^{1/3}\Delta\left(\gamma\phi^{-1/3}\right) \approx \frac{2}{R_I}\Delta\gamma \tag{25}$$

Eq. (25) shows that the simple spherical pore model yields zero adsorption stress $\Delta\boldsymbol{\sigma}_a$ due to the lack of coupling between A_s and external strain $\boldsymbol{\varepsilon}$. The first part of the second equation depicts a porosity-dependent adsorption pressure Δp_a, which is often a source of two-way adsorption-deformation coupling (Zhang, 2018). In the spirit of keeping the analytical solution explicit, we have made the approximation of $\phi \approx \phi_0$ to arrive at the last equation.

Attraction of fluid molecules onto the pore walls causes the fluid density to vary as depicted in Fig. 4. Gibbs surface excess convention lumps all the extra mass due to density variation near the solid pore surface onto a zero-thickness interface called surface excess phase (DeHoff, 2006), shown as the hatched area in Fig. 4. By doing so, the thermodynamic properties of the surface phase can be discussed. This leads to the celebrated Gibbs' adsorption isotherm (DeHoff, 2006):

$$d\gamma = -\Gamma^{surf}(\mu)\, d\mu \tag{26}$$

where Γ^{surf} is the surface excess number of moles per unit area, which is a function of partial pressure depicted by the adsorption isotherm; μ is the chemical potential of the adsorbate.

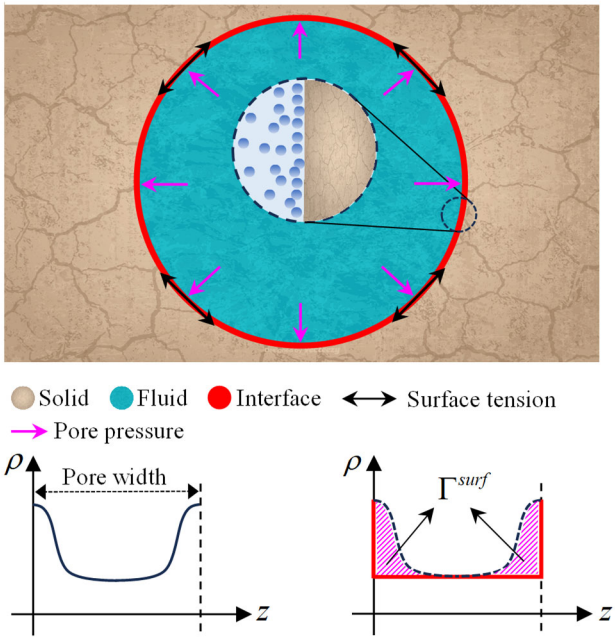

Fig. 4. Schematic of solid-fluid interface, adsorbed molecules, density variation of the fluid phase next to the solid and Gibbs' surface excess concept

In the current study, we focus on water vapor as the sole adsorbate gas. Its chemical potential can be expressed as a function of partial pressure p_w through Gibbs-Duhem equation for ideal gas (Ott and Boerio-Goates, 2000):

$$d\mu = \frac{R_g T}{p_w} dp_w \tag{27}$$

where $R_g = 8.314\,\mathrm{J}/\left(\mathrm{K}\times\mathrm{mol}\right)$ is the ideal gas constant and T is temperature in Kelvin.

Combining Eqs. (25), (26), and (27) gives the adsorption pressure as a function of relative humidity:

$$\Delta p_a(x) = -\frac{2R_g T}{R_l}\int_0^x \frac{\Gamma^{surf}(\bar{x})}{\bar{x}} d\bar{x} \tag{28}$$

where $x = p_w / p_{sat}$ is the relative humidity and p_{sat} is saturated vapor pressure; $\bar{x}$ is a dummy integration variable. Given that $\Gamma^{surf}(x)$ is a monotonically increasing function and notice Eq. (22), one can infer that the process of adsorption enhances the equivalent pore pressure ($p - \Delta p_a$) felt by the porous skeleton and thus promotes swelling of the overall REV.

Now we shall rewrite the surface poroelasticity (SP) model for the geometry and boundary conditions of the active porous layer in the bilayer system. Eliminating ($\phi - \phi_0$) in Eq. (22) gives:

$$\boldsymbol{\sigma} = \mathbf{C}^{\varepsilon} : \boldsymbol{\varepsilon} + \mathbf{C}^{\varepsilon\phi}(C^{\phi})^{-1}(p - \Delta p_a - \mathbf{C}^{\varepsilon\phi} : \boldsymbol{\varepsilon}) \tag{29}$$

Aligning directions 1, 2, and 3 with the $x - y - z$ coordinates shown in Fig. 2, the normal stresses can be expressed as:

$$\begin{aligned}
\sigma_x &= \left(K - \frac{2G}{3}\right)\left(\varepsilon_x + \varepsilon_y + \varepsilon_z\right) + 2G\varepsilon_x - b(p - \Delta p_a) \\
\sigma_y &= \left(K - \frac{2G}{3}\right)\left(\varepsilon_x + \varepsilon_y + \varepsilon_z\right) + 2G\varepsilon_y - b(p - \Delta p_a) \\
\sigma_z &= \left(K - \frac{2G}{3}\right)\left(\varepsilon_x + \varepsilon_y + \varepsilon_z\right) + 2G\varepsilon_z - b(p - \Delta p_a)
\end{aligned} \tag{30}$$

Substituting Eq. (2) into (30) and assuming constant atmospheric pressure p in the typical operation conditions of hydrostatic bilayers, one obtains the expression of misfit strain under free stress conditions:

$$\Delta\varepsilon = \varepsilon_x = -\frac{b}{3K}\Delta p_a \tag{31}$$

The curvature in hydroscopic bilayer can be readily obtained by substituting Eq. (31) into (1) and the resulting curvature can be then used in Eq. (15) to calculate the reaction force generated by the bilayer.

It is worth noting that the Clyne's solution Eq. (1) is derived based on the theory of elasticity where both layers are assumed linear elastic. In our model, the substrate layer is considered non-porous and is satisfactorily characterized by linear elasticity with $\left(E_b, \nu_b\right)$, while the top active porous layer is modeled here as a linear poroelastic material via Eq. (30). It is therefore necessary to establish linkage between the poroelastic and the elastic parameters for the top layer to ensure consistency. Since all bilayer experiments are conducted under pore-pressure controlled (drained) boundary conditions, the drained stiffnesses K and G are essentially identical to the bulk and shear modulus of the porous media as modelled by the linear elasticity theory. Therefore, the parameters for the top layer in Eq. (1) are conveniently linked with those in Eq. (30) via the usual relations between elastic constants (Sadd, 2009):

$$E_t = \frac{9KG}{3K+G}, \nu_t = \frac{3K-2G}{2\left(3K+G\right)} \tag{32}$$

The only remaining component to close the system is an adsorption isotherm $\Gamma^{surf}\left(x\right)$ needed in calculating the variation of adsorption pressure Δp_a. According to the IUPAC classification, there are six types of isotherms found in the experiments (Donohue and Aranovich, 1998). Many adsorption models have been proposed to describe gas adsorption on porous materials. The Langmuir (Langmuir, 1918) and BET (Brunauer et al., 1938) isotherms are the most referred ones in the literature. For micropore materials (pore size less than 2 nm), the adsorption data is satisfactorily described by the Langmuir equation which describes a monolayer adsorption process:

$$\Gamma^{surf} = \Gamma_0 \frac{cx}{1+cx} \tag{33}$$

where Γ_0 and c are Langmuir's parameters. On the other hand, BET isotherm is an extension of Langmuir isotherm to account for multilayer adsorption in mesoporous materials (pore size between 2 nm and 50 nm).

$$\Gamma^{surf} = \Gamma_0 \frac{cx}{(1-x)(1-x+cx)} \tag{34}$$

where c is a constant related to the heat of adsorption of first layer and the heat of liquefaction. Nonetheless, BET isotherm considers no structural limit on the number of adsorbed layers (i.e., unconstrained adsorption). In porous media, the outermost layers of adsorption on each side of the pore can influence each other, necessitating additional energy to account for these interactions. The BDDT isotherm (Brunauer et al., 1940) reflected such effect and is expressed as:

$$\Gamma^{surf} = \Gamma_0 \frac{c\,x}{1-x}\left[\frac{1+\left(\frac{1}{2}n\,g-n\right)x^{n-1}-\left(n\,g-n+1\right)x^{n}+\frac{1}{2}n\,g\,x^{n+1}}{1+\left(c-1\right)x+\left(\frac{1}{2}c\,g-c\right)x^{n}-\frac{1}{2}c\,g\,x^{n+1}}\right] \tag{35}$$

where all the parameters have the same meaning as in BET isotherm and g is the additional parameter related to the excess energy of evaporation of the last layer.

4. Model Validation

To validate the proposed analytical model, a finite element analysis (FEA) using ABAQUS software is performed to simulate the deformation and compute the tip reaction force of a hygroscopic bilayer. The surface poroelasticity model Eq. (22) together with the Langmuir isotherm Eq. (33) are implemented via a User Material (UMAT) subroutine to represent the porous layer, while the substrate is modeled by the ABAQUS built-in Hookean elasticity. The bilayer is initially configured as a quarter of a circle with a

length of 30 mm. Each layer has a thickness of 1 mm. Additional details regarding the model can be found in Appendix A. Fig. 5a compares the change of the mean curvature along the bilayer at different RH levels extracted from FE simulation and those obtained from analytical model Eq. (1). Additionally, the misfit strain is plotted alongside the curvature change in Fig. 5a, showing a variation between 0 – 1.3%. Note that misfit strain arises solely from surface poromechanics and are identical from both analytical and FEA calculations. Fig. 5b compares the reaction force at varying RH under fixed-end condition obtained by the FE simulation and the analytical model Eq. (15). The agreement between the two is excellent at all RH levels and for both boundary conditions, validating the presented model for a misfit strain of up to 1.3%. Our additional FE simulations, extended into the large-deformation regime, indicate that the analytical solutions (1) and (15) remain accurate up to a curvature change of 30 (1/m) with misfit strain approaching 4.5%. In the following, we shall employ the model for calibration and evaluate its predictive performance against real hygroscopic bilayer data, ensuring that its application remains within the FEA-validated strain levels.

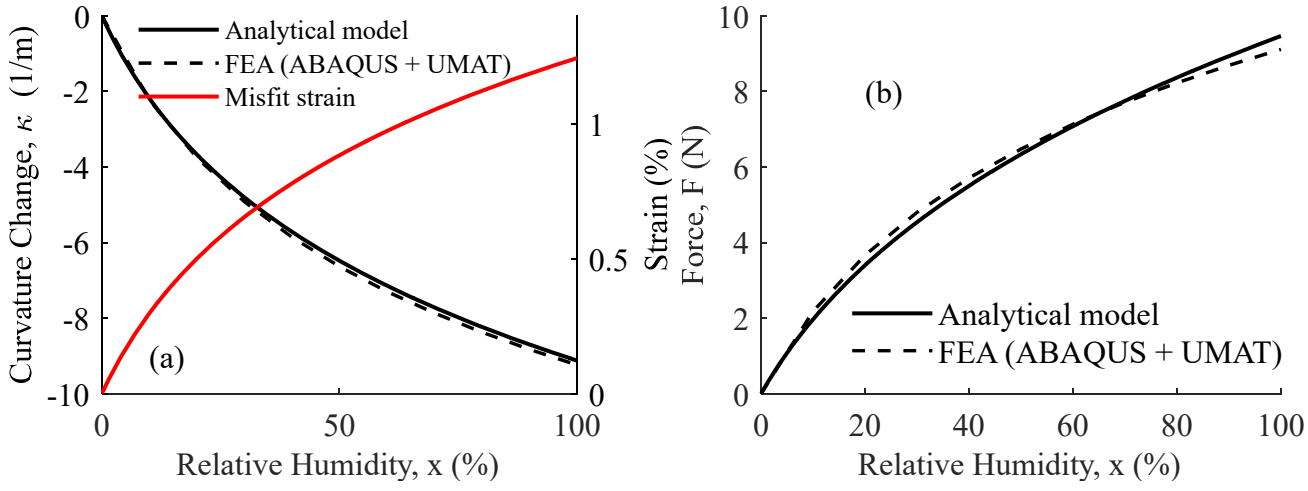

Fig. 5. (a) The change of mean curvature, misfit strain, and (b) the tip reaction force as functions of RH for an initially curved hygroscopic bilayer obtained by finite element analysis and the proposed analytical model.

5. Model performance

We conduct a case study on the hydroscopic bilayers produced and tested by Boudot et al. (2016). Their study involves two types of bilayers: one used an 80 nm thick microporous xerogel silica and the other used a 252 nm thick mesoporous silica as the active layer, both are deposited on a 50 μm thick inert polyimide substrate. Due to manufacturing process and the presence of residual stresses, the microporous xerogel silica and mesoporous silica bilayers exhibit an initial radius of curvature of 5.0 ± 0.3 cm and 6.8 ± 0.3 cm at 10% relative humidity toward the active layer, respectively. The bilayers were placed in a humidity-controlled chamber to assess their deformation and force generation as the relative humidity increased.

5.1. Adsorption isotherm

Let us first calibrate the adsorption isotherm parameters based on the data provided by Boudot et al. (2016). For consistency with the reported data, the adsorption isotherms should be expressed in terms of volumetric water content θ (volume of water in the pores divided by the total volume of the sample) instead of surface excess Γ^{surf}:

$$\theta = \frac{V_w}{V} = \frac{V_w}{V_v/\phi} = \frac{N^{surf} M/\rho_w}{\beta A_v R_I/\phi} \approx \frac{v_w \phi_0}{\beta R_I}\Gamma^{surf} \tag{36}$$

where V, V_v, V_w are the total volume of the REV, the volume of the void, and the equivalent volume of water, respectively; A_v is the total pore surface area; N^{surf} the total number of mole of the adsorbed water; $\rho_w = 998\,\mathrm{kg/m^3}$ the water density; $M = 18.015\,\mathrm{g/mol}$ the molar mass of water; $v_w = M/\rho_w = 18.05\,\mathrm{cm^3/mol}$ is molar volume of water; R_I the average radius of the pores; β is a shape factor linking the pore volume and pore surface area, which is set to 1/3 to be consistent with the spherical

pores assumption. We again assumed $\phi \approx \phi_0$ in accordance with Eq. (25) to facilitate explicit analytical solutions.

The adsorption data of micropores xerogel silica is shown in Fig. 6a. One can see that it is satisfactorily described by the Langmuir isotherm Eq. (33) through parameters presented in Table 1. The amount of adsorption approaches a plateau value at the end where the saturated state is reached. On the contrary, the adsorption data of mesoporous silica shown in Fig. 6b exhibits a sharp increase at around $RH = 70\%$, likely due capillary condensation in mesopores. Other than significantly increasing water content, capillary condensation leads to the formation of water meniscus in mesopores and can introduce volumetric shrinkage in the strain isotherm of the porous material (Barrer et al., 1956; Horikawa et al., 2011; Ohara et al., 2008; Restagno et al., 2000). Incorporating the physics of capillary condensation in surface poromechanics and reproducing condensation-induced contraction of mesoporous materials is beyond the scope here and will be rigorously pursued in our forthcoming studies. Here we shall focus on capturing the adsorption data of mesoporous silica through phenomenological isotherm models. Fig. 6b compares the data with Langmuir, BET, and BDDT isotherms (Eqs. (33) to (35)). Notably, the Langmuir isotherm is calibrated to fit the data in the pre-condensation regime but significantly deviates from the data at higher humidity levels. Although BET and BDDT isotherms are designed to describe multilayer adsorption processes, they are unable to satisfactorily replicate the adsorption data for mesoporous silica presented here. Their parameters are calibrated through the least squares fitting method and are reported in Table 1.

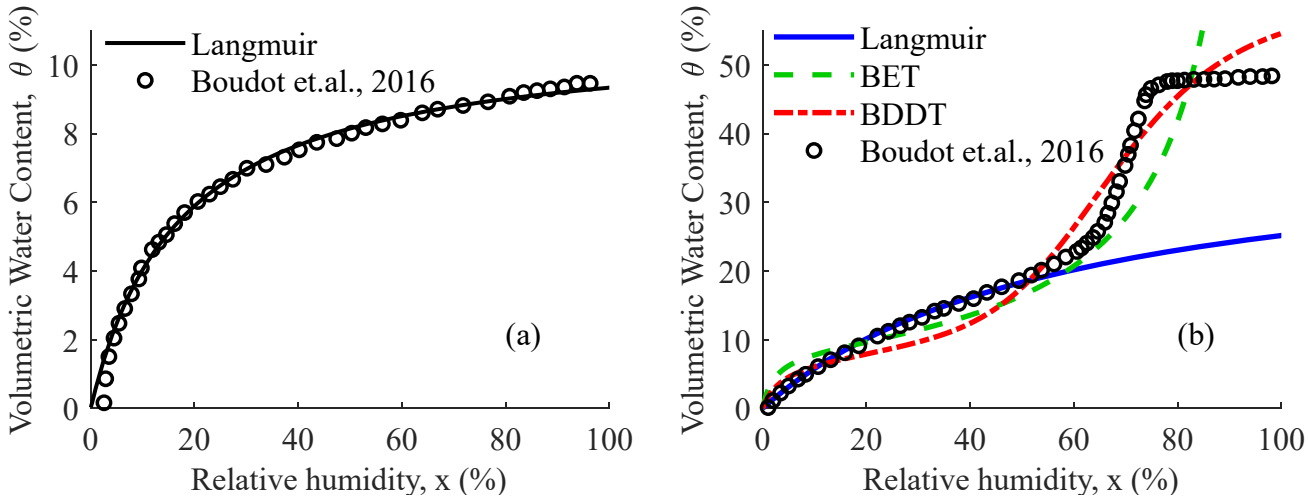

Fig. 6. Adsorption data and adsorption isotherms for (a) microporous xerogel silica and (b) mesoporous silica.

To enhance the modeling of the water adsorption data for mesoporous silica, we have explored several alternatives and found the Van Genuchten (1980) model to be promising. This model is designed to depict the water retention curve of unsaturated soils and has seen substantial applications in geotechnical and hydraulic engineering practices (Chang and Cheng, 2018; Likos and Yao, 2014; Luo et al., 2019). Assuming zero residual water content at high suctions, the Van Genuchten model is written as:

$$\theta = \frac{\theta_0}{\left[1+(\alpha\psi)^{1/(1-m)}\right]^m} \tag{37}$$

where θ_0 is the volumetric water content at full saturation; ψ is matric suction; α is related to the mean pore size of the porous medium; m denotes the breadth of pore size distribution. A porous material with a larger pore has bigger α, and a smaller m represents materials with broader pore size distribution (Benson et al., 2014) in which capillary condensation happens more smoothly. Matric suction ψ, also known as capillary pressure (Moghadam et al., 2020), is the pressure difference between two immiscible fluids. At equilibrium, suction and relative humidity is linked through the Kelvin's law (Coussy, 2004):

$$\psi = -\frac{R_g T}{v_w}\ln(x) \tag{38}$$

Substituting Eq. (38) into Eq. (37) gives the Van Genuchten (VG) water retention curve (WRC) in terms of relative humidity.

$$\theta = \theta_0\left[1+\left(\frac{\alpha R_g T}{v_w}\ln(x)\right)^{1/(1-m)}\right]^{-m} \tag{39}$$

The VG model can robustly capture the rapid increase in water content in the capillary condensation regime at mid-to-high humidity levels. However, it does not account for the adsorption of water molecules on the pore walls prior to condensation at low humidity levels. Observing the complementary features of Langmuir and VG models, it is possible to construct a new isotherm model, namely the L-VG isotherm, that additively combines the two models to cover the full range of adsorption data for mesoporous solid:

$$\theta = \frac{v_w\phi}{\beta R_I}\Gamma_0\frac{cx}{1+cx} + \theta_0\left[1+\left(\frac{\alpha R_g T}{v_w}\ln(x)\right)^{1/(1-m)}\right]^{-m} \tag{40}$$

Fig. 7 depicts the L-VG isotherm Eq. (40) along with its Langmuir and VG components which correspond to the first and the second term on the left-hand side of Eq. (40), respectively. The parameters, calibrated using the least-squares method, are listed in Table 1. One can see that the L-VG isotherm effectively captures the data in both the adsorption-dominant and post-condensation regimes. For the particular data we are looking at, approximately half of the water content at saturation is attributed to adsorption, while the remaining portion arises from capillary condensation. The L-VG isotherm appears as a robust and flexible four-parameter adsorption model for mesoporous materials across the full range of humidity levels.

Table 1

Parameters for adsorption isotherms.

	Γ_0 (mol/m^2)	c	g	n	m	α (1/Pa)	θ_0
Langmuir	2.020e-5	5.832	-	-	-	-	-
BET	1.554e-5	43.937		-	-	-	-
BDDT	7.474e-6	28.024	63.280	8.365	-	-	-
L-VG	4.150e-5	1.691	-	-	0.906	2e-8	0.245

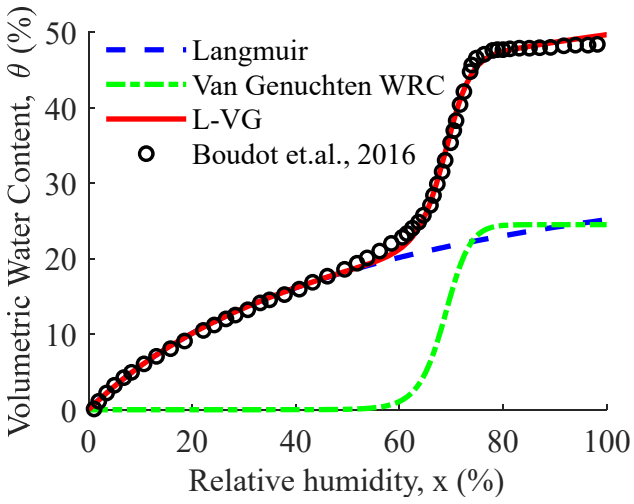

Fig. 7. The adsorption data of mesoporous silica interpreted by L-VG isotherm.

5.2. Curvature change

With the adsorption isotherm calibrated, we now can compute the misfit strain, and the subsequent curvature change in the hygroscopic bilayer by combining Eqs. (1), (3), (28), (31), and the isotherm models. The elastic properties of microporous xerogel silica and mesoporous silica can be found in literature and are summarized

Table **2** (Abramoff and Klein, 1990; Dourdain et al., 2008; Gross et al., 1988; Patil et al., 2017). The Biot coefficient can be expressed as $b = 1 - K / K_s$ for an ideal porous medium (Cheng, 2016), where K is the

drained bulk modulus of overall REV and K_s is the bulk modulus of solid phase. The latter is, however, not reported in past experimental studies. Hence, b is selected to best fit the curvature evolutions, and this calibrated value will be used to predict force generation in fixed-end configurations.

Table 2

Parameters for microporous and mesoporous bilayers.

	Geometry				Poroelasticity					Microstructure	
	h (nm)	H (μm)	L (mm)	b_w (mm)	E_t (GPa)	ν_t	E_b (GPa)	ν_b	b	ϕ_0	R_I (nm)
Microporous bilayer	80	50	30	6	4.5	0.22	2.5	0.3	0.54	0.1	1
Mesoporous bilayer	252	50	30	6	4.5	0.22	2.5	0.3	0.34	0.49	2.75

Fig. 8a and b show the calculated and the measured radius of curvature versus relative humidity for the microporous and the mesoporous bilayers, respectively. It is observed from Fig. 8a that the surface poroelasticity (SP) model with Langmuir isotherm performed exceptionally well for microporous bilayer with $R^2 = 0.9788$. Fig. 8b suggests that, when combining SP with the four isotherms, the L-VG model provides a central trendline, accommodating most of the data points in both pre- and post- condensation regime with the highest R^2 value of 0.8680. The Langmuir model coincides with the L-VG curve at low RH regime but severely diverges at high RH levels with an overall $R^2 = 0.7701$. The BET isotherm highly overestimates the data at $RH < 80\%$ with $R^2 = 0.6978$. Although BDDT isotherm predicted similar curvature as the L-VG, its prediction for $RH < 40\%$ tends to be higher than that of L-VG the with slightly lower R^2 value of 0.8623. Overall, all four models somewhat underpredicted the curvature of mesoporous bilayer at $RH > 80\%$. This suggests that the adsorption-deformation mechanism is no longer dominated by the reduction of the solid-fluid interfacial energy (i.e., Bangham effect) at high RH levels for

mesoporous materials. Other mechanisms such as capillary condensation and the dynamic evolution of liquid-vapor interface in mesopores must be introduced in future extensions of the constitutive theory.

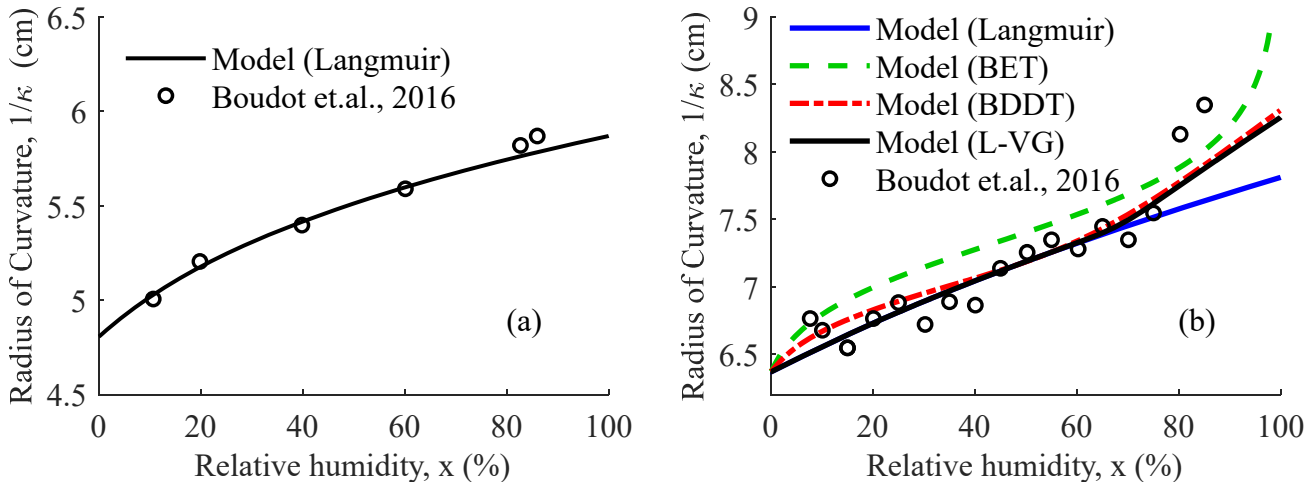

Fig. 8. Measured v.s predicted radius of curvature by (a) microporous silica and (b) mesoporous silica xerogel bilayers.

5.3. Reaction force

The force generated by a fixed-end hygroscopic bilayer under humidity change can be computed by combining Eqs. (1), (3), (15), (28), (31), and a suitable isotherm model. The same model parameters calibrated for curvature data in Table 2 are used here for reaction force predictions. Fig. 9a and b show the calculated and the measured force generated versus relative humidity for the microporous and the mesoporous bilayers, respectively. The reaction force in the microporous bilayer (Fig. 9a) is predicted as a useful central trend line, capturing the overall pattern of force increase with relative humidity, showing a slight overestimation at low RH and underestimation at high RH levels. For the mesoporous bilayer (Fig. 9b), similar conclusions can be drawn as from Fig. 8b: The Langmuir isotherm cannot capture the data post-condensation ($R^2 = 0.9266$) as expected, while the BET isotherm grossly overpredicted the reaction force ($R^2 = 0.6531$). The BDDT and L-VG isotherms provide the best agreements with the experimental data with R^2 values of 0.9438 and 0.9722, respectively. However, the BDDT isotherm overestimated the

reaction force at low RH regime, making the L-VG isotherm the most favorable model. It is worth noting that the reaction force data is not monotonic for mesoporous bilayers, with a marked reduction at $RH \approx 80\%$. Such non-monotonic trend may also exist in Fig. 8b but inseparable with data scatters. This phenomenon may be linked with the capillary condensation-induced contraction behavior of mesoporous solids as discussed in Section 4.1. Extending the surface poromechanics theory of Zhang (2018) for unsaturated mesoporous media can potentially address this gap and will be pursued in a follow-up study.

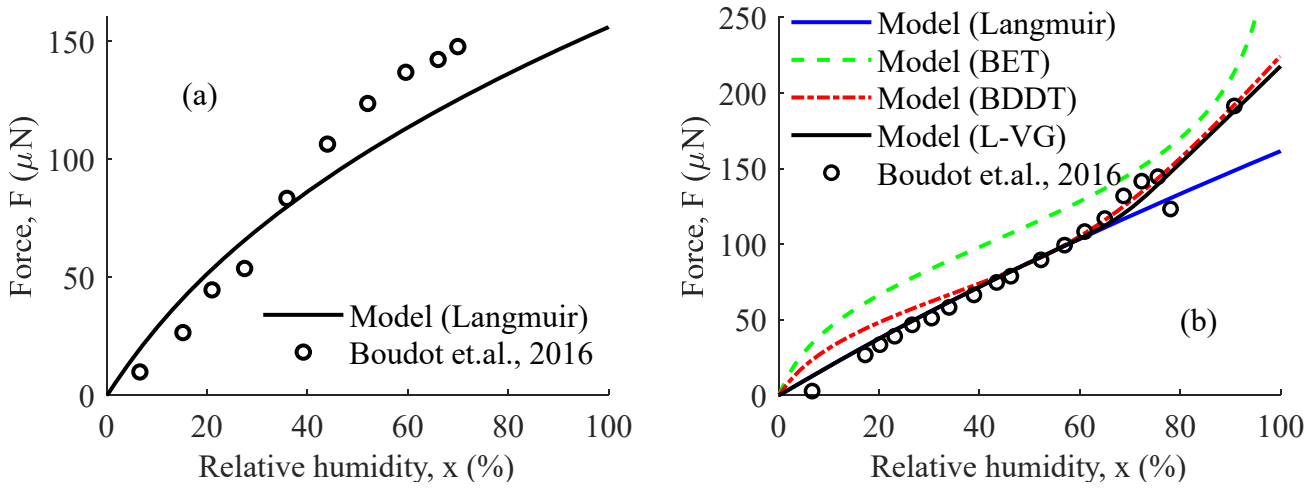

Fig. 9. Measured vs. predicted reaction force by (a) microporous silica and (b) mesopore silica xerogel bilayers.

6. Discussions

The previous section demonstrated that the proposed analytical solutions can satisfactorily predict the curvature and force development of hygroscopic bilayers upon adsorption. We shall continue to explore other aspects of the model and perform preliminary parametric studies for optimized bilayer designs.

6.1. Derivation of Bilayer's shape change from curvature evolution

Taking the curvature of a curve at every point as input, the full geometry of the curve can be obtained by performing integration along the s-coordinate. We outlined a discrete mathematical scheme in Appendix A to determine the shape of the deformed bilayer at different humidity levels. Fig. 10a and b depict the

458 predicted shape evolutions of the microporous and mesoporous bilayers using the Langmuir and the L-
459 VG isotherms, respectively. They compare very well with the actual specimen images provided by Boudot
460 et al. (2016). A closer inspection of the photos suggests that the curvature in the real bilayer slightly
461 changes along the length as opposite to the uniform curvature predicted by the model. This might be
462 attributed to the intrinsic assumption in the Clyne's solution (Eq. (1)) that zero shear stress exists along
463 the adhesive interface, resulting in pure bending and thus a constant curvature along the bilayer beam.
464 Notably, the microporous bilayer (with 10% porosity) and the mesoporous bilayer (with 49% porosity)
465 exhibit comparable deformation (see Fig. 10). This may be attributed to the surface area available for
466 adsorption which itself is a function of porosity, pore size and thickness of the responsive layer. An
467 increase in porosity and thickness and a decrease in pore size independently is expected to result in higher
468 adsorption and larger swellings. Here, the adsorption capacity in a thin microporous coating with low
469 porosity is compensated by its smaller pore size, making it comparable to that of a thicker mesoporous
470 coating with higher porosity. The maximum misfit strain is 1.22% and 0.38% with tip rotation of 6.4° and
471 6.1° at saturation for microporous and mesoporous bilayers, respectively. These values are reasonably
472 small and are below the FEA validated misfit strain level of 1.3%, making the use of the proposed
473 analytical model appropriate.

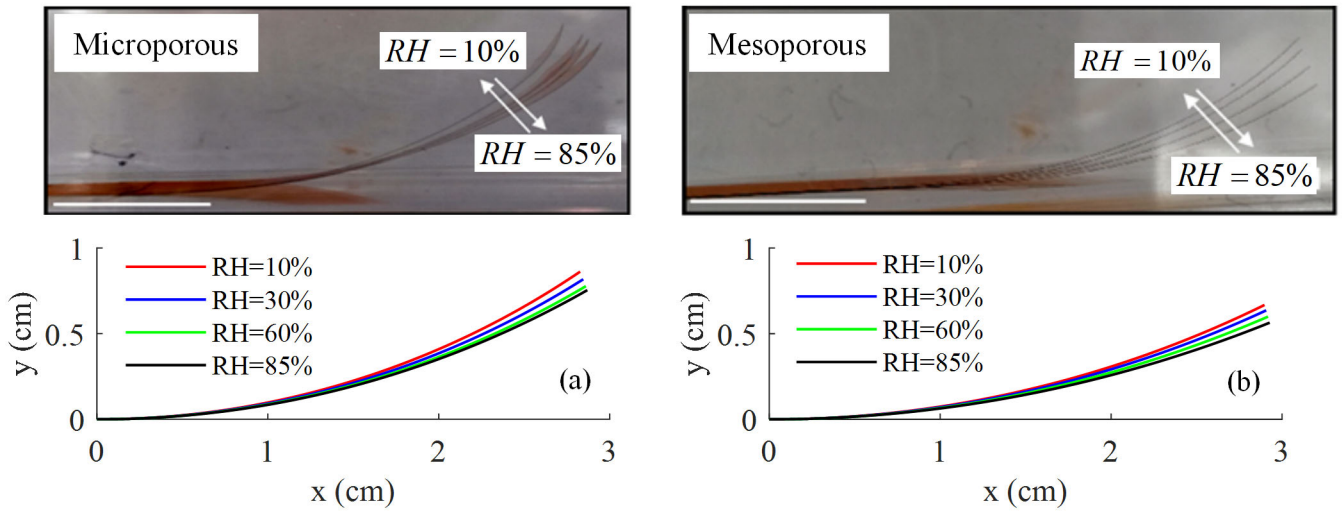

Fig. 10. Comparision of the bilayer shape reported by Boudot et al. (2016) and predicted by the model at RH ranging from 10% to 85% for (a) microporous silica and (b) mesoporous silica xerogel coatings.

6.2. Effect of substrate's elastic property and coating thickness

Revolving around a specific porous material, the freedom in designing hygroscopic bilayers often lies in varying the substrate materials to achieve different substrate Young's moduli and adjusting the thickness of the active porous layer. Here we perform a parametric study on these two factors assuming a mesoporous coating. The model parameters associated with the mesoporous silica reported in Table 1 and Table **2** are used as the baseline parameters. To augment the shape evolution, the initial shape of bilayer is assumed to be a half-circle with radius of curvature of $\pi / L = 104.72\,\mathrm{m}^{-1}$ at $RH = 0\%$, as shown in dash lines in Fig. 11a. The final shape at $RH = 100\%$ for $E_b = 30\,\mathrm{MPa} - 2.5\,\mathrm{GPa}$ are shown in solid lines in Fig. 11a. The evolution of radius of curvature and reaction force with respect to increasing RH are reported in Fig. 11b and c, respectively. We can see from Fig. 11b that a softer substrate gives larger curvature change upon adsorption under free-end condition, as expected. Interestingly, in fixed-end scenarios (Fig. 11c) for the chosen parameters, while softer substrate generates weaker reaction forces in the low-RH regime, this pattern completely reverses as RH approaches 100%. This can be attributed to the fact that the more compliant bilayer can produce more pronounced curvature change (as observed in

the free-end scenario) at high RH levels, outweighing its relatively low overall stiffness. The non-monotonic relation between the reaction force and the substrate stiffness has important implications for the design of hydroscopic actuators. For actuators intended to operate at low-mid RH levels, a stiffer substrate can optimize the force output. Conversely, a more compliant bilayer system is preferred if the operating environment varies from dry to near saturation.

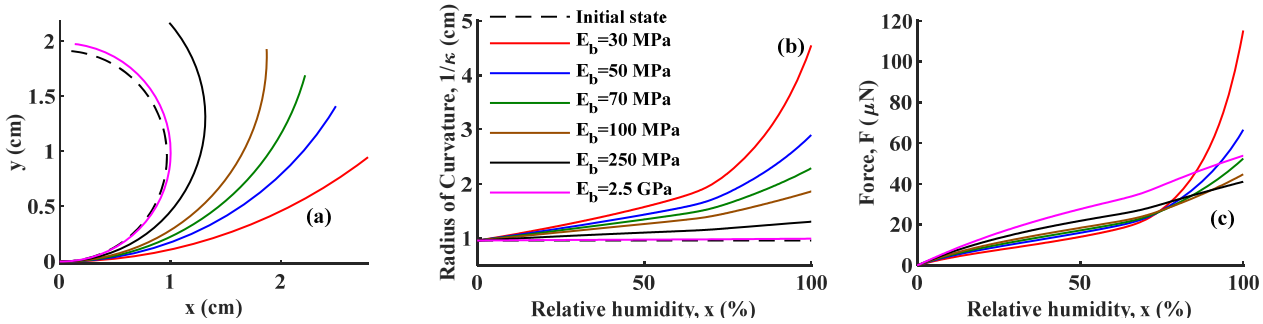

Fig. 11. Effect of Young's modulus of the substrate on the (a) shape, (b) curvature, and (c) reaction force of the bilayer.

The thickness of the porous coating is another important design parameter for hygroscopic bilayers. Using the same baseline parameters, Fig. 12a, b and c report the change of shape at fully saturation, and curvature, and reaction force from $RH = 0\%$ to $RH = 100\%$ for different coating thickness ($h = 100\,\text{nm} - 2\,\mu\text{m}$), respectively. It can be inferred from Fig. 12a and b that increasing the thickness of the active porous layer leads to an improvement in the deformation magnitude. This suggests that, although an increase in thickness of the active layer can result in a stiffer bilayer system, the adsorption-induced swelling of a thicker active layer outweighs the former and produces a larger magnitude of hygroscopic movement. For fixed-end scenarios, Fig. 12c advises that an increased coating thickness and thus a higher overall stiffness results in a greater force output.

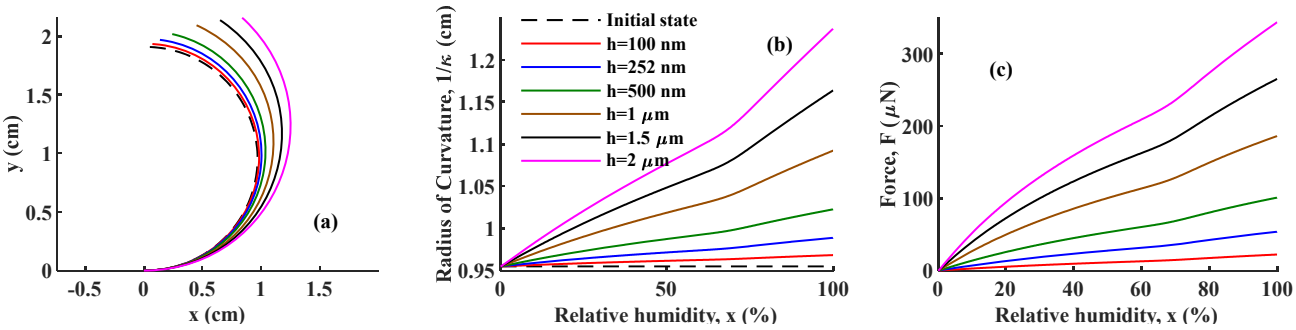

Fig. 12. Effect of thickness of the active layer on the (a) shape, (b) curvature, and (c) reaction force of the bilayer.

7. Conclusion

In this study, we derived an analytical solution for the response of a hygroscopic bilayer subjected to humidity variation. Clyne (1995) simple bilayer beam theory was employed to calculate the curvature change due to the misfit strain under free-end conditions. Based on Castigliano's second theorem, the force generated by a fixed-end cantilever bilayer beam was derived. An adsorption-deformation constitutive model based on surface poromechanics (Zhang, 2018) was presented and utilized to derive an expression for the misfit strain. As part of the model input, the Langmuir, BET, and BDDT adsorption isotherms together with a newly proposed L-VG adsorption model are introduced to complete our analytical solution for the moisture-driven curvature and force generations of hygroscopic bilayers. A mathematical scheme is proposed to reconstruct the shape of the bilayer for given curvature data. The model is validated through experimental data on microporous and mesoporous bilayers provided by Boudot et al. (2016). A parametric study is carried out using the proposed analytical model to explore how the substrate's Young's modulus and the coating thickness influence the performance of hygroscopic bilayers, offering important insights for their design. The main conclusions of this study are summarized as follows:

1) We revisited the Clyne's bilayer bending solution and developed a new equation for calculating the reaction force generated by a misfit strain in generic stimuli-responsive bilayers. Comparison

against finite element simulations confirmed the robustness and accuracy of the solutions for small-strain applications.

2) Adsorption-induced swelling of the active porous layer can be effectively described by a surface poroelasticity model when paired with appropriate adsorption isotherms. Combining the predicted misfit strain with the analytical model provides accurate descriptions of the behavior of microporous and mesoporous bilayers observed in experiments.

3) The newly proposed L-VG adsorption isotherm, which accounts for both adsorption and condensation contributions, more accurately captures the sorption curve of mesoporous materials compared to the Langmuir, BET, and BDDT isotherms. For microporous materials, the Langmuir isotherm is sufficient to describe the sorption response.

4) Our parametric study using the proposed analytical model revealed a complex relationship between bilayer performance and substrate stiffness. Optimal values for substrate stiffness can be determined based on the design objectives – whether maximizing curvature change or reaction forces – and the operating RH ranges. Additionally, a thicker porous layer leads to increased reaction forces and curvature changes.

It is also important to note several assumptions and limitations of the proposed analytical model. The selected constitutive models for the top and bottom layers have assumed linearity and isotropy. This may affect the model's accuracy for extremely compliant bilayer systems with pronounced deformations (geometrical nonlinearity) and with material anisotropy. Clyne's solution predicts a uniform curvature along the bilayer beam, which may differ from actual bilayer responses, where curvature can vary slightly along the length. This aspect may be addressed by incorporating more realistic assumptions regarding the interactions (normal and shear stresses) between the substrate and the coating, as well as heterogeneity of the materials. Finally, fundamentally incorporating the physics of capillary condensation in surface

poromechanics theory is needed to capture the shrinkage and subsequent expansion of mesoporous materials at mid/high RH levels. This will enable the model to more accurately depict the curvature and force response of mesoporous bilayers in post-condensation regime.

Acknowledgment

This research was funded by the U.S. National Science Foundation (NSF) under NSF CMMI Award No. 2113474 and the U.S. Department of Energy (DOE) through Grant DE-SC0024391.

Data Availability Statement

The ABAQUS package that supports the findings of this study are available in the supplementary material of this article.

Declaration of Competing Interest

The authors declare that they have no known competing financial interests or personal relationships that could have appeared to influence the work reported in this paper.

References

Abramoff, B., Klein, L.C., 1990. Elastic Properties of Silica Xerogels. Journal of the American Ceramic Society 73, 3466-3469.

Alameen, E.H., Lucantonio, A., DeSimone, A., 2023. Mechanics and transient morphing of soft hygroscopic bilayers. Mechanics Research Communications 131, 104131.

Armon, S., Efrati, E., Kupferman, R., Sharon, E., 2011. Geometry and mechanics in the opening of chiral seed pods. Science 333, 1726-1730.

Bakhshian, S., Sahimi, M., 2017. Adsorption-induced swelling of porous media. International Journal of Greenhouse Gas Control 57, 1-13.

Bangham, D.H., Fakhoury, N., 1928. The expansion of charcoal accompanying sorption of gases and vapours. Nature 122, 681-682.

Barrer, R.M., McKenzie, N., Reay, J.S.S., 1956. Capillary condensation in single pores. Journal of Colloid Science 11, 479-495.

Benítez, A.J., Torres-Rendon, J., Poutanen, M., Walther, A., 2013. Humidity and Multiscale Structure Govern Mechanical Properties and Deformation Modes in Films of Native Cellulose Nanofibrils. Biomacromolecules 14, 4497-4506.

Benson, C., Chiang, I., Chalermyanont, T., Sawangsuriya, A., 2014. Estimating van Genuchten Parameters α and n for Clean Sands from Particle Size Distribution Data.

Biot, M.A., 1941. General theory of three-dimensional consolidation. Journal of applied physics 12, 155-164.

Boudot, M., Elettro, H., Grosso, D., 2016. Converting water adsorption and capillary condensation in usable forces with simple porous inorganic thin films. ACS nano 10, 10031-10040.

Brunauer, S., Deming, L.S., Deming, W.E., Teller, E., 1940. On a theory of the van der Waals adsorption of gases. Journal of the American Chemical society 62, 1723-1732.

Brunauer, S., Emmett, P.H., Teller, E., 1938. Adsorption of gases in multimolecular layers. Journal of the American chemical society 60, 309-319.

Chang, C., Cheng, D.-H., 2018. Predicting the soil water retention curve from the particle size distribution based on a pore space geometry containing slit-shaped spaces. Hydrology and Earth System Sciences 22, 4621-4632.

Cheng, A.H.D., 2016. Micromechanics, in: Cheng, A.H.D. (Ed.), Poroelasticity. Springer International Publishing, Cham, pp. 83-112.

Clyne, T.W., 1995. Residual stresses in surface coatings and their effects on interfacial debonding. Key engineering materials 116, 307-330.

Correa, D., Poppinga, S., Mylo, M.D., Westermeier, A.S., Bruchmann, B., Menges, A., Speck, T., 2020. 4D pine scale: biomimetic 4D printed autonomous scale and flap structures capable of multi-phase movement. Philosophical Transactions of the Royal Society A: Mathematical, Physical and Engineering Sciences 378, 20190445-20190445.

Coussy, O., 2004. Poromechanics. John Wiley & Sons.

Dąbrowski, A., 2001. Adsorption — from theory to practice. Advances in Colloid and Interface Science 93, 135-224.

DeHoff, R., 2006. Thermodynamics in materials science. CRC Press.

Donohue, M.D., Aranovich, G.L., 1998. Classification of Gibbs adsorption isotherms. Advances in Colloid and Interface Science 76-77, 137-152.

Dourdain, S., Britton, D., Reichert, H., Gibaud, A., 2008. Determination of the elastic modulus of mesoporous silica thin films by x-ray reflectivity via the capillary condensation of water. Applied Physics Letters 93.
Eskandari-Ghadi, M., Zhang, Y., 2021. Mechanics of shrinkage-swelling transition of microporous materials at the initial stage of adsorption. International Journal of Solids and Structures 222, 111041-111041.
Eskandari-Ghadi, M., Zhang, Y., 2022. Effect of pore size distribution on sorption-induced deformation of porous materials: A theoretical study. International Journal of Solids and Structures 242, 111533-111533.
Flory, P.J., Rehner, J., 1943. Statistical mechanics of cross-linked polymer networks II. Swelling. Journal of Chemical Physics 11, 521-526.
Gross, J., Reichenauer, G., Fricke, J., 1988. Mechanical properties of SiO2 aerogels. Journal of Physics D: Applied Physics 21, 1447.
Harrington, M.J., Razghandi, K., Ditsch, F., Guiducci, L., Rueggeberg, M., Dunlop, J.W., Fratzl, P., Neinhuis, C., Burgert, I., 2011. Origami-like unfolding of hydro-actuated ice plant seed capsules. Nature communications 2, 337.
Hibbeler, R.C., 2006. Structural Analysis.
Higueras-Ruiz, D., Nishikawa, K., Feigenbaum, H., Shafer, M., 2021. What is an artificial muscle? A comparison of soft actuators to biological muscles. Bioinspiration & Biomimetics 17.
Hong, W., Zhao, X., Zhou, J., Suo, Z., 2008. A theory of coupled diffusion and large deformation in polymeric gels. Journal of the Mechanics and Physics of Solids 56, 1779-1793.
Horikawa, T., Do, D.D., Nicholson, D., 2011. Capillary condensation of adsorbates in porous materials. Advances in Colloid and Interface Science 169, 40-58.
Khoshtinat, S., Carvelli, V., Marano, C., 2023. Cellulose acetate for a humidity-responsive self-actuator bilayer composite. Cellulose 30, 7779-7790.
Krüger, F., Thierer, R., Tahouni, Y., Sachse, R., Wood, D., Menges, A., Bischoff, M., Rühe, J., 2021. Development of a Material Design Space for 4D-Printed Bio-Inspired Hygroscopically Actuated Bilayer Structures with Unequal Effective Layer Widths. Biomimetics 6, 58.
Langmuir, I., 1918. The adsorption of gases on plane surfaces of glass, mica and platinum. Journal of the American Chemical Society 40, 1361-1403.
Li, S., Wang, K., 2016. Plant-inspired adaptive structures and materials for morphing and actuation: a review. Bioinspiration & biomimetics 12, 011001.
Likos, W.J., Yao, J., 2014. Effects of Constraints on van Genuchten Parameters for Modeling Soil-Water Characteristic Curves. Journal of Geotechnical and Geoenvironmental Engineering 140, 06014013-06014013.
Luo, Z., Kong, J., Shen, C., Lu, C., Hua, G., Zhao, Z., Zhao, H., Li, L., 2019. Evaluation and application of the modified van Genuchten function for unsaturated porous media. Journal of Hydrology 571, 279-287.
Menges, A., 2012. HygroScope.. Meteorosensitive Morphology. Arch Plus, 7.
Moghadam, A., Vaisblat, N., Harris, N.B., Chalaturnyk, R., 2020. On the magnitude of capillary pressure (suction potential) in tight rocks. Journal of Petroleum Science and Engineering 190, 107133-107133.
Montero de Espinosa, L., Meesorn, W., Moatsou, D., Weder, C., 2017. Bioinspired polymer systems with stimuli-responsive mechanical properties. Chemical reviews 117, 12851-12892.
Ohara, S., Adschiri, T., Ida, T., Yashima, M., Mikayama, T., Abe, H., Setsuhara, Y., Nogi, K., Miyahara, M., Kaneko, K., Ohtomo, A., 2008. Chapter 5 - Characterization methods for nanostructure of

materials, in: Hosokawa, M., Nogi, K., Naito, M., Yokoyama, T. (Eds.), Nanoparticle Technology Handbook. Elsevier, Amsterdam, pp. 267-315.
Ott, J.B., Boerio-Goates, J., 2000. Chapter 6 - Fugacity, Activity, and Standard States, in: Ott, J.B., Boerio-Goates, J. (Eds.), Chemical Thermodynamics: Principles and Applications. Academic Press, London, pp. 247-323.
Patil, S.P., Rege, A., Sagardas, Itskov, M., Markert, B., 2017. Mechanics of Nanostructured Porous Silica Aerogel Resulting from Molecular Dynamics Simulations. The Journal of Physical Chemistry B 121, 5660-5668.
Pini, R., Ottiger, S., Burlini, L., Storti, G., Mazzotti, M., 2009. Role of adsorption and swelling on the dynamics of gas injection in coal. Journal of Geophysical Research (Solid Earth) 114, B04203-B04203.
Restagno, F., Bocquet, L., Biben, T., Charlaix, É., 2000. Thermally activated dynamics of capillary condensation. Journal of Physics: Condensed Matter 12, A419.
Reyssat, E., Mahadevan, L., 2009. Hygromorphs: from pine cones to biomimetic bilayers. Journal of the Royal Society Interface 6, 951-957.
Sadd, M.H., 2009. Elasticity: theory, applications, and numerics. Academic Press.
Shin, B., Ha, J., Lee, M., Park, K., Park, G.H., Choi, T.H., Cho, K.-J., Kim, H.-Y., 2018. Hygrobot: A self-locomotive ratcheted actuator powered by environmental humidity. Science Robotics 3, eaar2629-eaar2629.
Shuttleworth, R., 1950. The surface tension of solids. Proceedings of the physical society. Section A 63, 444.
Suo, Z., 2007. Poroelasticity, or diffusion in an elastic solid.
Sydney Gladman, A., Matsumoto, E.A., Nuzzo, R.G., Mahadevan, L., Lewis, J.A., 2016. Biomimetic 4D printing. Nature Materials 15, 413-418.
Timoshenko, S., 1925. Analysis of bi-metal thermostats. Josa 11, 233-255.
Van Genuchten, M.T., 1980. A closed - form equation for predicting the hydraulic conductivity of unsaturated soils. Soil science society of America journal 44, 892-898.
Vandamme, M., Brochard, L., Lecampion, B., Coussy, O., 2010. Adsorption and Strain: The CO2-Induced Swelling of Coal. Journal of The Mechanics and Physics of Solids - J MECH PHYS SOLIDS 58, 1489-1505.
Wang, W., Yao, L., Cheng, C.-Y., Zhang, T., Atsumi, H., Wang, L., Wang, G., Anilionyte, O., Steiner, H., Ou, J., Zhou, K., Wawrousek, C., Petrecca, K., Belcher, A.M., Karnik, R., Zhao, X., Wang, D.I.C., Ishii, H., 2017. Harnessing the hygroscopic and biofluorescent behaviors of genetically tractable microbial cells to design biohybrid wearables. Science Advances 3, e1601984.
Zhang, Y., 2018. Mechanics of adsorption–deformation coupling in porous media. Journal of the Mechanics and Physics of Solids 114, 31-54.
Zhao, Q., Dunlop, J.W.C., Qiu, X., Huang, F., Zhang, Z., Heyda, J., Dzubiella, J., Antonietti, M., Yuan, J., 2014. An instant multi-responsive porous polymer actuator driven by solvent molecule sorption. Nature Communications 5, 4293-4293.
Zhao, X., Hong, W., Suo, Z., 2008. Stretching and polarizing a dielectric gel immersed in a solvent. International Journal of Solids and Structures 45, 4021-4031.
Zhou, X., Liu, S., Zhang, Y., 2021. Permeability evolution of fractured sorptive geomaterials: a theoretical study on coalbed methane reservoir. Rock Mechanics and Rock Engineering 54, 3507-3525.

Appendix A. ABAQUS Implementation

A hygroscopic bilayer, initially shaped as a quarter circle with a length of 30 mm, was simulated using the ABAQUS software. The thickness is divided into four elements, with the top two assigned as the responsive material and the bottom two serving as the substrate. The FEA mesh consists of a total of 2784 C3D8 elements with an approximated global size of 0.0005. The proposed surface poroelasticity model is assigned to the top layer through a User Material (UMAT) subroutine. The ABAQUS built-in linear isotropic elasticity is assigned to the bottom layer. The same material parameters used for modeling Boudot et al. (2016)'s microporous bilayer given in Table 1 and

Table **2** are assigned in the present FE model. The relative humidity within the bilayer linearly and uniformly increases from 0 to 1 as a function of pseudo time, enforced through the UMAT subroutine. In other words, our simulations focus on equilibrium states, without accounting for the transient diffusion of water vapor into the bilayers.

Two types of simulations were conducted: the first type allowed the tip to remain unconstrained to simulate curvature change, while the second type constrained the horizontal displacement of the tip to calculate the force generated by the bilayer. Due to symmetry in Fig. 2, half of the bilayer is modeled with one end being fixed (encastre). The simulation was conducted over 1000 steps, with each step incrementing relative humidity by 0.1%. The procedure type is Static, General with Nlgeom set to off due to small deformations. The simplicity of the constitutive model enabled convergence in a single iteration at each step, allowing the simulation to be completed on a standard laptop in just a few minutes. The readers are encouraged to build and develop their own model and conduct the respective simulation. The UMAT code and the ABAQUS input file can be found in the supplementary materials of this paper.

For the free-end case, after the simulation is completed, nodal displacement data at the interface of two layers are extracted and post-processed to calculate the mean curvature values at different relative

humidities, with increments of 10% (Fig. 5a). For the fixed-end case, the reaction force at the tip node is directly monitored and reported (Fig. 5b). Fig 13 depicts the deformed hygroscopic bilayer FE model at $RH = 100\%$, along with the mesh and boundary conditions used in the free-end simulations.

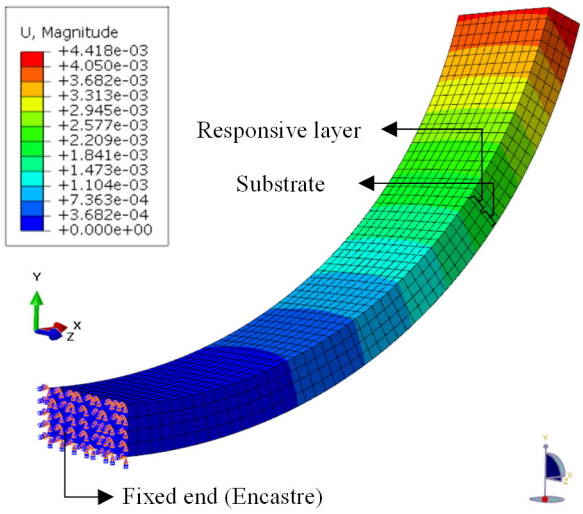

Fig. 13. The deformed bilayer modeled in ABAQUS at RH=100%.

Appendix B. Discrete method to obtain the curve shape

Curvature is defined as the rate of change of the tangent vector as one moves along a smooth curve:

$$\kappa = \frac{\|d\mathbf{T}\|}{\|d\mathbf{S}\|} \tag{41}$$

where $d\mathbf{T}$ and $d\mathbf{S}$ are increments of the tangent and the position vectors on the curve, respectively; $\|\bullet\|$ is Euclidean norm. According to Fig. 14, if two points $\mathbf{P}_1$ and $\mathbf{P}_2$ with tangent unit vector $\mathbf{T}_1$ and $\mathbf{T}_2$ respectively exist on the curve and are sufficiently close to each other, we can assume that

$$\|d\,\mathbf{T}\| \approx d\theta \tag{42}$$

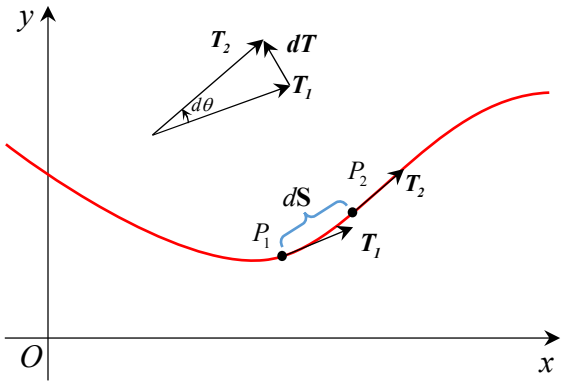

728

729 *Fig. 14. The piecewise linear method approximates the shape of an arbitrary curve by utilizing the known curvature at each point.*

730 Combining Eqs. (41) and (42) gives

731 $$d\theta = \kappa \left\| d\mathbf{S} \right\| \tag{43}$$

732 Given the coordinate, the curvature, and the tangent at the point $\mathbf{P}_1$, it is possible to find the coordinate

733 and the tangent at point $\mathbf{P}_2$ in terms of the increment $\left\| d\mathbf{S} \right\|$ between the two points:

734 $$\mathbf{P}_2 = \mathbf{P}_1 + \left\| d\mathbf{S} \right\| \mathbf{T}_1 \tag{44}$$

735 Choosing adequately small $\left\| d\mathbf{S} \right\|$ yields to a sufficiently precise determination of the location for point $\mathbf{P}_2$

736 . According to Fig. 14, a rotation in tangent $\mathbf{T}_1$ with amount of $d\theta$ results in $\mathbf{T}_2$ in which the rotation is

737 considered to have the same sign as the curvature.

738 $$\mathbf{T}_2 = \mathbf{R} \cdot \mathbf{T}_1 \tag{45}$$

739 where $\left[\mathbf{R} \right] = \begin{bmatrix} \cos(d\theta) & -\sin(d\theta) \\ \sin(d\theta) & \cos(d\theta) \end{bmatrix}$ is the rotation matrix.

740